energies

MDPI

Article

Performance Assessment of an $NH_3/LiNO_3$ Bubble Plate Absorber Applying a Semi-Empirical Model and Artificial Neural Networks

Carlos Amaris [1,2], Maria E. Alvarez [3], Manel Vallès [1] and Mahmoud Bourouis [1,*]

[1] Department of Mechanical Engineering, Universitat Rovira i Virgili, Av. Països Catalans No. 26, 43007 Tarragona, Spain; Camaris5@cuc.edu.co (C.A.); manel.valles@urv.cat (M.V.)
[2] Department of Energy, Universidad de la Costa, Cl. 58 #55-66, Barranquilla 080002, Colombia
[3] School of Chemical Engineering, Universidad Metropolitana, Av. Boyacá, Carcacas-Miranda 1073, Venezuela; mealvarez@unimet.edu.ve
* Correspondence: mahmoud.bourouis@urv.cat

Received: 9 July 2020; Accepted: 17 August 2020; Published: 20 August 2020

Abstract: In this study, ammonia vapor absorption with $NH_3/LiNO_3$ was assessed using correlations derived from a semi-empirical model, and artificial neural networks (ANNs). The absorption process was studied in an H-type corrugated plate absorber working in bubble mode under the conditions of an absorption chiller machine driven by low-temperature heat sources. The semi-empirical model is based on discretized heat and mass balances, and heat and mass transfer correlations, proposed and developed from experimental data. The ANN model consists of five trained artificial neurons, six inputs (inlet flows and temperatures, solution pressure, and concentration), and three outputs (absorption mass flux, and solution heat and mass transfer coefficients). The semi-empirical model allows estimation of temperatures and concentration along the absorber, in addition to overall heat and mass transfer. Furthermore, the ANN design estimates overall heat and mass transfer without the need for internal details of the absorption phenomenon and thermophysical properties. Results show that the semi-empirical model predicts the absorption mass flux and heat flow with maximum errors of 15.8% and 12.5%, respectively. Maximum errors of the ANN model are 10.8% and 11.3% for the mass flux and thermal load, respectively.

Keywords: bubble absorption; plate heat exchanger; advanced surfaces; heat and mass transfer correlations; semi-empirical model; artificial neural networks; ammonia; lithium nitrate

1. Introduction

Absorption cooling systems appear to be promising energy-saving technologies if they use residual/available heat or solar energy for their operation [1]. However, actual absorption equipment with traditional working mixtures has a number of limitations. To overcome the inconvenience and restrictions of traditional working mixtures, one option suggested in the open literature is the use of $NH_3/LiNO_3$ [2,3]. The most attractive aspect of absorption systems using a $NH_3/LiNO_3$ mixture is that they can be cooled by air because crystallisation does not occur at high condensation temperatures. In addition, systems with a $NH_3/LiNO_3$ mixture do not require rectification of the refrigerant vapor emitted from the generator because the absorbent is a salt, and these systems can operate at lower activation temperatures compared to ammonia/water (NH_3/H_2O) systems. Nevertheless, former experimental investigations have shown that the major limiting aspect of the $NH_3/LiNO_3$ mixture is its elevated viscosity, which restricts heat and mass transfer, primarily in the absorber, in comparison to the NH_3/H_2O mixture [4–7]. This limitation has motivated studies aimed at enhancing the absorption process with $NH_3/LiNO_3$ by employing passive techniques [8–10]. A

comprehensive review of experimental studies involving vapor absorption intensification using passive methods for absorption cooling/heating systems was also recently published [1].

Absorbers can have various configurations depending on their operation mode, including falling film absorbers, bubble absorbers, spray absorbers, or membrane absorbers. The first two of these configurations are the most commonly used in absorption cooling/heating systems available in the market [1]. Moreover, various studies have concluded that bubble absorbers contribute to (i) larger heat and mass transfer, (ii) superior interface contact between the refrigerant and weak solution, and (iii) simpler absorber design, compared to those in falling film mode [11,12]. This configuration also allows smaller designs for a given system capacity.

Numerical models devoted to studying the absorption process in various designs have been reported to provide a more detailed comprehension of the processes that take place in bubble mode absorbers. However, numerical studies of the absorption process in $NH_3/LiNO_3$ bubble absorbers and correlations are scarce [13,14]. For instance, Infante Ferreira [13] addressed numerical and experimental studies in a vertical tubular absorber for $NH_3/LiNO_3$ and NH_3/NaSCN mixtures. The numerical model included Nusselt's theory and penetration theory to assess the heat and mass transfer parameters. The main result of the study showed that the relationship between the predicted and experimental mass transfer coefficients ranged between 0.64 and 1.60. Moreover, Cerezo et al. [14] theoretically modelled the absorption phenomenon in a plate heat exchanger (PHE) involving L-type internal corrugations with NH_3/H_2O, $NH_3/LiNO_3$, and NH_3/NaSCN mixtures. The authors presented a study comparing the performance of the absorber with these three working fluids. Temperatures and thermal load profiles along the absorber were presented for each case study.

Numerical approaches of the bubble absorption process with other working fluids are also available in the literature. Investigations using the conventional working pair of H_2O/LiBr were not included in this literature review because this fluid mixture is commonly used in falling film mode absorbers and requires low vacuum pressure conditions for the absorption process. Moreover, various authors have focused on the absorber performance with NH_3/H_2O as a working fluid in a range of absorber configurations such as vertical tubular bubble absorbers [15–17], a plate absorber with offset strip fins (OSF) [11,18], a cylindrical bubble absorber [19], a shell and tubes type bubble absorber [16], and an L-type plate absorber [20]. Some of these studies required the use of local heat and mass transfer equations for the vapor and liquid phase, in addition to equations for the vapor bubble diameter, the bubble velocity, and the gas hold-up [11,15,18–20]. Other absorber modelling studies including the use of mixtures such as ionic liquids [21] and R22-DMF, R22-DMA, R22-DMETEG, R22-DMEDEG, and R22-NMP [22,23] have also been reported in the literature.

In general, studies devoted to detailing the flow characteristics, bubble formation, and rise in bubble absorbers for various working fluids reached several conclusions [24–32]: (i) the dominant heat transfer resistance is mainly located in the mixture side; (ii) the mass transfer decreases along the length of the absorber as solution approaches the saturation conditions; and (iii) the vapor phase conditions have an insignificant effect on the absorption process in comparison to effects of solution concentration, temperature, coolant temperature, tube diameter, and length [11,16,18].

The artificial neural network (ANN) design also appears to be an interesting technique for modeling thermal systems. ANNs operate as black-box models and are intended to imitate the biological process of the brain which can be trained to perform an activity. A small number of studies involving the use of ANNs have been published in the open literature [33–36]. For instance, Kalogirou [33] reported various ANN model designs to estimate the capability of renewable energy system configurations. Chow et al. [37] designed an absorption chiller control system based on an ANN and genetic algorithms. Hernández et al. [38] used an ANN to predict the performance of a heat transformer system for water purification. Subsequently, Labus et al. [39] developed an ANN model to simulate the performance of a low-capacity absorption refrigeration machine. Lastly, Alvarez et al. [40] developed an ANN model to assess the performance parameters of a horizontal falling film absorber with aqueous (lithium, potassium, sodium) nitrate solutions.

Based on the literature review, no validated semi-empirical heat and mass transfer models exist in the open literature to predict the NH_3 bubble absorption in an H-type corrugated PHE with $NH_3/LiNO_3$ mixture. The present study was part of an R&D project investigating the characterization of the absorption process with $NH_3/LiNO_3$. The aim was to improve the information available about the performance of $NH_3/LiNO_3$ bubble absorbers and contribute to their technological development. Therefore, this paper aims to provide a description and validation of dimensionless correlations and two different models developed to predict the performance of the NH_3 absorption process in a bubble plate absorber. The first model developed is based on discretized heat and mass balances in addition to empirical heat and mass transfer correlations fitted from experimental data, whereas the second model is based on trained artificial neural networks. Initially, each model is assessed and validated individually. Then, a performance comparison between both models is conducted. Finally, the advantages of each model are presented.

2. Methodology

This study involved the proposal of correlations generated from the experimental characterization of the absorption process of ammonia vapor, development of two model options to predict the NH_3 absorption process in a bubble plate absorber, validation of both models, and comparison of the results. The key details of the experimental test setup are presented in the next sub-section. The first model is a semi-empirical model detailed in Section 2.2, while the second model is an artificial neural networks-based model described in Section 2.3.

2.1. Experimental Setup

Figure 1 shows the experimental setup used to assess and correlate the ammonia vapor absorption in a plate heat exchanger. In this facility, measurable variables, such as inlet flows, inlet temperatures, inlet solution concentration in ammonia, and inlet solution pressure in the test section, can be monitored and controlled. The facility consists of 3 circuits: the $NH_3/LiNO_3$ mixture circuit, the heating circuit, and the heat dissipation/cooling circuit. In the $NH_3/LiNO_3$ mixture circuit, the solution (weak in refrigerant) is pumped (B1) from the storage tank 1 (ST1) to the heat exchanger (SHE) where it reaches the required solution temperature at the test section inlet. After the absorption process takes place in the test section, the solution (strong in refrigerant) leaves the test section to flow to a vapor–liquid separator (VLS) and finally to the storage tank 2 (ST2). The heating circuit includes a 5 kW heater (R1), a water–water heat exchanger (HX2), a pump (B2), and a magnetic flow meter (F). The heat dissipation/cooling circuit is used to dissipate the excess of heat released during the absorption process in the test section. This circuit includes a 5 kW heater (R2), a magnetic flow meter (F), a pump (B3), and a heat exchanger (HX1). The test section is also connected to an ammonia bottle which supplies the ammonia vapor at a pressure slightly higher than that in the absorber inlet.

Various measuring devices were used for data monitoring and collection. Figure 1 shows the location of instrumentation such as sensors for temperature (T) and pressure (P), and magnetic (F) and Coriolis flowmeters (C). The data collection began after the ammonia vapor injection and once the steady-state was reached in the thermal conditions of the flows. Data was collected every 5 s for around 15 min.

The absorber used for this study was a plate heat exchanger (PHE) with four braze plates (three channels). The PHE is made of stainless steel AISI 316 and provided by Alfa Laval. It has Chevron-H type corrugations which correspond to an angle of 30° from the horizontal axis.

The operation of the absorber is in counter-current flow. The $NH_3/LiNO_3$ mixture and ammonia vapor flow upward in the inner channel while the cooling-water flows downward in the side channels. For more details of the PHE, please see Table 1 and Figure 2. More details about the experimental procedure and test facility are given by Amaris in [41].

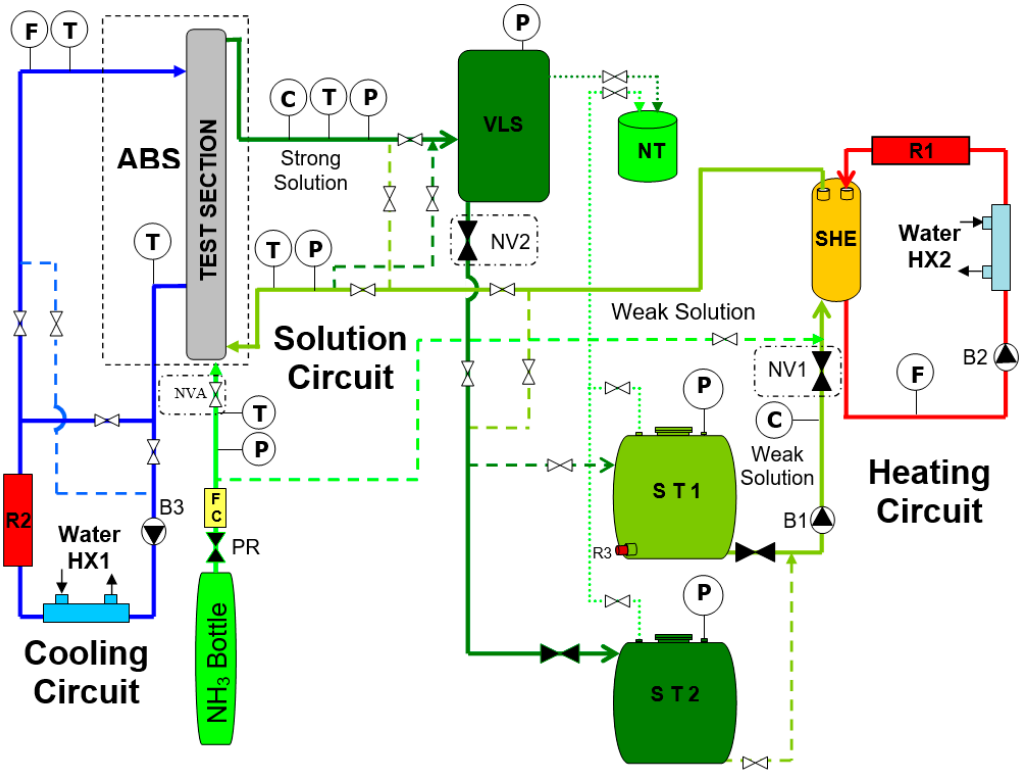

Figure 1. Scheme of the experimental equipment.

Table 1. Specifications of the plate heat exchanger (PHE).

Plate Heat Exchanger	
Corrugation	**Type H**
Length, m	0.53
Width, m	0.112
Area of heat exchange, m^2	0.1
Hydraulic diameter of the channels, m	0.004
Thickness of the plate, m	0.0004

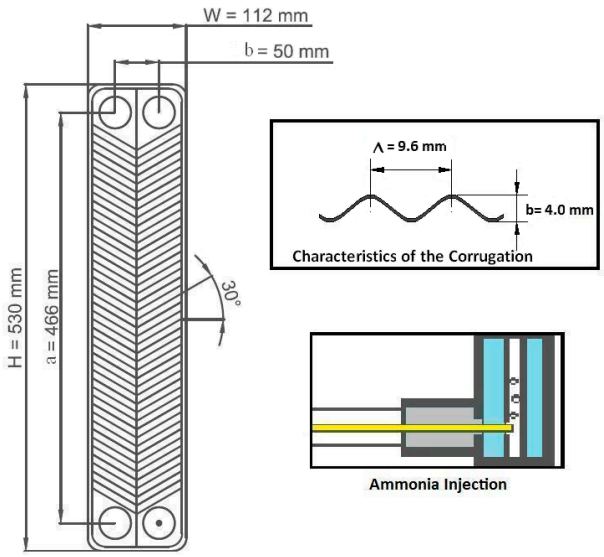

Figure 2. Main details of the H-type PHE.

The nominal operating conditions of the present application are shown in Table 2. These conditions of operation correspond to those of a simple-effect absorption chiller driven by low-temperature heat and a chilled-water temperature of 5 °C.

Table 2. Operating conditions at the inlet of the PHE.

Parameters	Range
Solution temperature, °C	45
Water-side temperature, °C	35, 40
Ammonia mass fraction in solution, $kg_{NH_3} \cdot kg^{-1}{}_{NH_3/LiNO_3}$	0.45
Solution-side pressure, kPa	510
Solution-side mass flow, $kg \cdot h^{-1}$	10–70
Water volumetric flow, $m^3 \cdot h^{-1}$	0.130–0.450

2.2. Semi-Empirical Model

A semi-empirical model was developed to predict the performance of the $NH_3/LiNO_3$ bubble plate absorber. Modelling of the absorption process was carried out by the discretization of the PHE in small volumes of control. In each volume of control, energy and mass balances were solved at the same time as the simulation advanced progressively from the inlet to the outlet of the PHE (see Figure 3).

The $NH_3/LiNO_3$ thermodynamic properties reported by Libotean et al. [42,43] and Cuenca et al. [44] were implemented in the model. The enthalpy values were determined according to the method proposed by Haltenberger [45] and implemented by McNeely [46].

The main considerations for the development of the model are presented below:

- Model in one dimension and steady-state conditions,
- Pressure drop is negligible,
- Equal heat and mass transfer areas,
- Refrigerant temperature equal to the inlet solution temperature,
- Adiabatic exterior border.

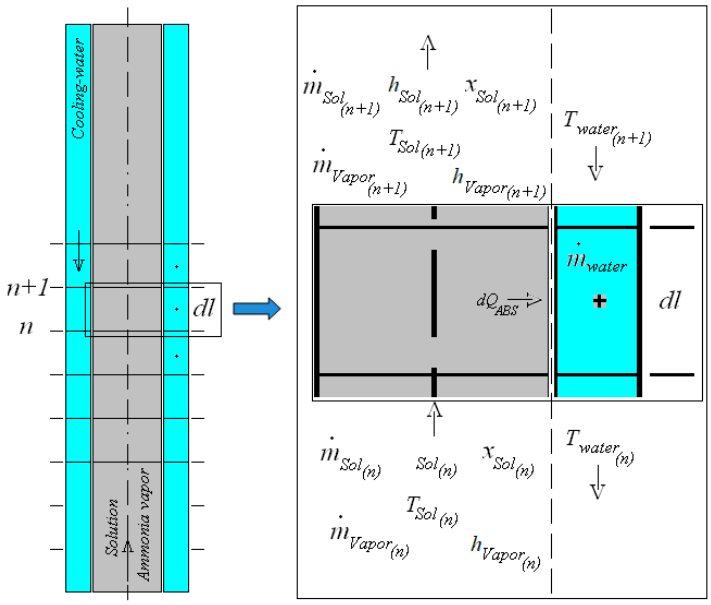

Figure 3. Geometric discretization of the bubble absorber.

2.2.1. Discretized Governing Equations and Correlations

The numerical model relies basically on heat and mass balances, heat and mass transfer correlations, and equations for the thermodynamic properties of the solution and water flows.

The heat and mass balances and correlations are described as follows:
Solution-side global mass balance:

$$\dot{m}_{Sol}(n+1) + \dot{m}_{Vap}(n+1) - \dot{m}_{Sol}(n) - \dot{m}_{Vap}(n) = 0 \quad (1)$$

Solution-side partial mass balance:

$$\dot{m}_{Sol}(n+1) \cdot x_{Sol}(n+1) - \dot{m}_{Sol}(n) \cdot x_{Sol}(n) - d\dot{m}_{Sol} = 0 \quad (2)$$

$$d\dot{m}_{Sol} = -d\dot{m}_{AB\_Vap} \quad (3)$$

$$d\dot{m}_{Sol} = F_{AB} \cdot dTa \quad (4)$$

where $d\dot{m}_{Sol}$ is the differential mass transfer in each control volume, F_{AB} is the NH_3 absorption mass flux, and dTa is the differential transfer area. dTa is determined as $dTa = 2{\cdot}w{\cdot}dl$, where w is the width of the plate while dl is the control volume differential length. F_{AB} is determined from Equation (5) where k_m is the mass transfer coefficient and $LMXD$ is the logarithmic mean concentration difference. k_m is determined from Equation (6) where the Sh_{Sol} is approached by Equation (16). In Equation (6), β_{Sol} is the diffusivity of the $NH_3/LiNO_3$ which is estimated as in [47].

$$K_m = \frac{F_{AB}}{LMXD} \quad (5)$$

$$Sh_{Sol} = \frac{K_m \cdot D_h}{\beta_{Sol}} \quad (6)$$

Solution-side energy balance:

$$\dot{m}_{Sol}(n){\cdot}h_{Sol}(n) + \dot{m}_{Vap}(n){\cdot}h_{Vap}(n) - \dot{m}_{Sol}(n+1){\cdot}h_{Sol}(n+1) - \dot{m}_{Vap}(n+1){\cdot}h_{Vap}(n+1) = d\dot{Q}_{AB} \quad (7)$$

The thermal load ($d\dot{Q}_{AB}$) is approached as follows:

$$d\dot{Q}_{AB} = U \cdot dTa \cdot (T_{Sol}(n) - T_{Cw}(n)) \quad (8)$$

The temperature of the water flow at the outlet of each control volume is determined from:

$$d\dot{Q}_{AB} = \dot{m}_{Cw} \cdot Cp_{Cw} \cdot [T_{Cw}(n+1) - T_{Cw}(n)] \quad (9)$$

The overall heat transfer coefficient (U) is estimated considering the resistances for the heat flow in each volume of control:

$$\frac{1}{U} = \frac{1}{\alpha_{Sol}} + \frac{e}{\lambda_{Steel}} + \frac{1}{\alpha_{Cw}} \quad (10)$$

where α_{Sol} represents the solution heat transfer coefficient and α_{Cw} is the water-side heat transfer coefficient. The heat transfer coefficients are estimated as follows:

$$\alpha_{Sol} = \frac{Nu_{Sol} \cdot \lambda_{Sol}}{D_{h\_Sol\_Side}} \quad (11)$$

$$\alpha_{Cw} = \frac{Nu_{Cw} \cdot \lambda_{Cw}}{D_{h\_Cw\_Side}} \quad (12)$$

where λ represents the thermal conductivity of each fluid and D_h refers to the hydraulic diameter in each side, estimated as $4 \times Ap/Pw$ and simplified to 2 times the plate separation. In this case, the

hydraulic diameter is the same for both sides. The solution-side Nusselt number (Nu_{Sol}) and water-side Nusselt number (Nu_{Cw}) were estimated using the correlations proposed in Section 3.1.

2.2.2. Model Resolution

The numerical model follows a sequential resolution of heat and mass balances in every control volume beginning from the first control volume to the last.

Because the PHE absorber operates in counter-current configuration, the outlet water-side temperature is initially assumed by the model, while the outlet bulk solution conditions and inlet water-side conditions in each control volume are estimated from the heat and mass balances. The simulation finishes when the estimated inlet water-side temperature reaches the actual inlet water-side temperature. The code of the numerical model was written in the Engineering Equation Solver (EES) software.

The model simulation procedure is as follows:

- Input of the absorber geometrical characteristics.
- Input of inlet operating conditions such as: $T_{Sol}(n)$, $x_{Sol}(n)$, $m_{Sol}(n)$, $P_{Sol}(n)$, $m_{Vap}(n)$, T_{Cw}, $V_{Cw}(n)$, and $P_{Cw}(n)$.
- The model guesses an initial outlet water-side temperature $T_{Cw}(n)$.
- Evaluation of the first control volume:
    - Estimation of thermodynamic properties.
    - Estimation of Sh_{Sol}, k_m, F_{AB} and mass transfer balances in the control volume.
    - Estimation of α_{Sol}, α_{Cw}, $T_{Sol}(n+1)$, $T_{Cw}(n+1)$, and energy balances.

  The model guesses $T_{Sol}(n+1)$, carries out energy balances, and calculates $T_{Cw}(n+1)$. If balances are close, the simulation runs on the next control volume, else, a new $T_{Sol}(n+1)$ is assumed. $T_{Sol}(n+1)$ is set by applying the secant method.
- When the simulation reaches the last control volume, the calculated $T_{Cw}(n+1)$ is compared to the actual T_{Cw}. The simulation finishes if values are equal, else, a new $T_{Cw}(n)$ is guessed, and the simulation starts again from the first control volume. $T_{Cw}(n)$ is estimated by applying the secant method.

2.3. Artificial Neural Networks Model

The ANN requires input and output information so that training and therefore, the learning process, can take place. The ANN consists of 3 layers: an input layer, a hidden layer, and an output layer. The hidden layer is the heart of the ANN and consists of processing units called neurons. These neurons are grouped and linked to other layers by interconnections called weights. The input layer collects the input data while the output layer reproduces the required data from the network as an output. The required neurons in the hidden layer are defined by the prediction accuracy of the required parameters. Consequently, there are no explicit guidelines to define the design of the ANN structure. The network responses to the input data are the transfer functions at the outlet of each neuron. The hyperbolic tangent sigmoid function (tansig) is the most commonly used transfer function (Equation (13)) in the hidden layer while the linear transfer function (purelin) is used in the output layer (Equation (14)):

$$f(x) = \frac{2}{1 + exp(-2x)} - 1 \tag{13}$$

$$f(x) = x \tag{14}$$

Normalization of the input data was required to avoid any influence of the magnitude of input values in the defined ranges of the experimentation. Therefore, inputs were normalized within the range from 0.1 to 0.9 by Equation (15) [48]:

$$P_i = 0.8 * \left(\frac{I_i - I_{min}}{I_{max} - I_{min}} \right) + 0.1 \quad (15)$$

The neurons in the input and output layers correspond to the input and output parameters. The back-propagation method employing the Levenberg–Marquardt optimization algorithm was used to compare the experimental data feeding the network and the target output. Obtaining an accurate and solid ANN depends on the input parameters, the information available, and the method employed for training [48]. An experimental set of data was previously collected from the absorption process of ammonia vapor in an H-type plate absorber with $NH_3/LiNO_3$ [41].

The inlet parameters of the PHE, P_{Sol}, T_{Cw}, V_{Cw}, m_{Sol}, T_{Sol}, and x_{Sol}, were set as input data to the ANN. Previously, experimental data collection was conducted at a x_{Sol} of 0.45 with a total of 30 experiments according to the procedure described in Section 2.1. From the available information, 17 experiments corresponded to a heat dissipation temperature of 35 °C, and 13 experiments to a heat dissipation temperature of 40 °C. In every set of experiments, some parameters were kept constant while others were varied. The following information was employed for the design of the ANN: Inlet values from 0.01389 to 0.00289 kg·s^{-1} for $\dot{m}_{Sol}$, from 0.450 to 0.1312 m^3·h^{-1} for V_{Cw}, and from 40.8 to 34.9 °C for T_{Cw}. The ANN design was developed using the neural network application of MATLAB software.

3. Results and Discussion

This section presents the correlations proposed, and results from the semi-empirical and ANN models developed to quantify the performance parameters of NH_3 bubble absorption with a $NH_3/LiNO_3$ mixture. The validation and comparison of both models with experimental data are also reported.

3.1. Heat and Mass Transfer Correlations

This sub-section presents the heat and mass transfer correlations developed and proposed considering the data collected by Amaris [41] from an experimental study of the H-type PHE absorber. Correlations in Equations (16) and (17) correspond to the solution Nusselt (Nu_{Sol}) and Sherwood (Sh_{Sol}) numbers that characterize the absorption process. Validations of these correlations are presented in Figure 4. Moreover, correlation in Equation (18) refers to the water-side Nusselt number (Nu_{Cw}) also obtained from the performance of the H-type PHE using water in both the inner and side channels. This means that prior to the experimental investigation of the ammonia absorption process, a preliminary heat transfer experimental study was conducted using water in the inner and side channels. Results from this study are reported Equation (18) and Figure 5.

The solution Nusselt, Sherwood, and water-side Nusselt numbers were correlated by reducing the mean square error (MSE) when contrasting the correlated and experimentally estimated dimensionless parameters. Variables such as the inlet heat dissipation water temperature, inlet solution temperature, and solution equilibrium temperature were found to have a significant effect on the heat and mass transfer. Therefore, they were included in the correlation to account for these effects [49].

$$Sh_{Sol} = 872358 \cdot Re_{Sol}^{0.51} \cdot Sc_{Sol}^{-1.08} \cdot \left(\frac{T_{Sol,Eq,in}}{T_{Sol,in}} \right)^{3.87} \cdot \left(\frac{T_{Sol,in}}{T_{Cw,in}} \right)^{2.97} \quad (16)$$

$$\mathrm{Nu}_{Sol} = 1.24 \cdot Re_{Sol}^{0.6} \cdot Pr_{Sol}^{1/3} \cdot \left(\frac{T_{Sol,Eq,in}}{T_{Sol,in}} \right)^{1.12} \cdot \left(\frac{T_{Sol,in}}{T_{Cw,in}} \right)^{-1.41} \quad (17)$$

$$Nu_{Cw} = 0.858 \cdot Re_{Cw}^{0.555} \cdot Pr_{Cw}^{1/3} \quad (18)$$

Figure 4b demonstrates that Equation (16) can adequately estimate 90% of the solution mass transfer coefficient points with relative differences below 15%. Moreover, Equation (17) can estimate 90% of the solution heat transfer coefficient data with relative differences below 15% (see Figure 4a). These correlations estimate the experimental data with average relative differences of 6.6% and 7.3%, for the heat and mass transfer coefficients, respectively. The fit parameter R^2 for each correlation is shown in Figure 4. The correlations proposed in Equations (16) and (17) were developed for Reynolds numbers ranging from 10 to 55. In this study, the Prandtl number ranged between 46 and 51, and the Schmidt number in Equation (16) ranged from 5194 to 5947.

Figure 5a,b shows the overall heat transfer coefficient and water-side Nusselt number (Nu_{Cw}) obtained from the experimental study in the H-type PHE using water in both channels in counter-current configuration and correlated in Equation (15). The black line represents the trend of the results. In these experiments, temperatures were changed in a range from 30 to 60 °C while the mass flow was varied from 50 to 352 kg·h^{-1}. The correlation proposed in Equation (18) is recommended for a water turbulent flow with a Reynolds number ranging from 400 to 1400. The Prandtl number for the water flow ranged between 4.20 and 4.75. Figure 5a shows that Equation (18) can satisfactorily estimate 82.4% of the overall water heat transfer coefficient data with relative differences below 2% and an average relative difference of 1.17%.

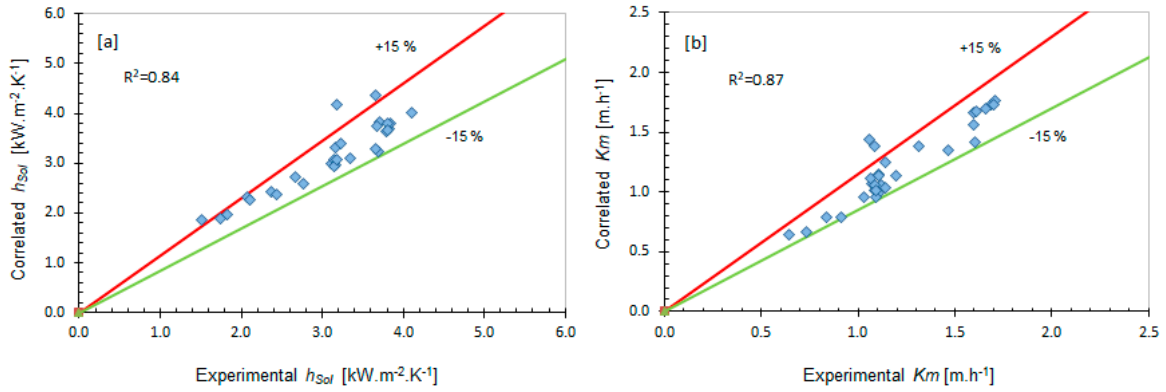

Figure 4. Predicted data vs. experimental data in the H-type PHE for (**a**) solution-side heat transfer coefficient; and (**b**) solution-side mass transfer coefficient.

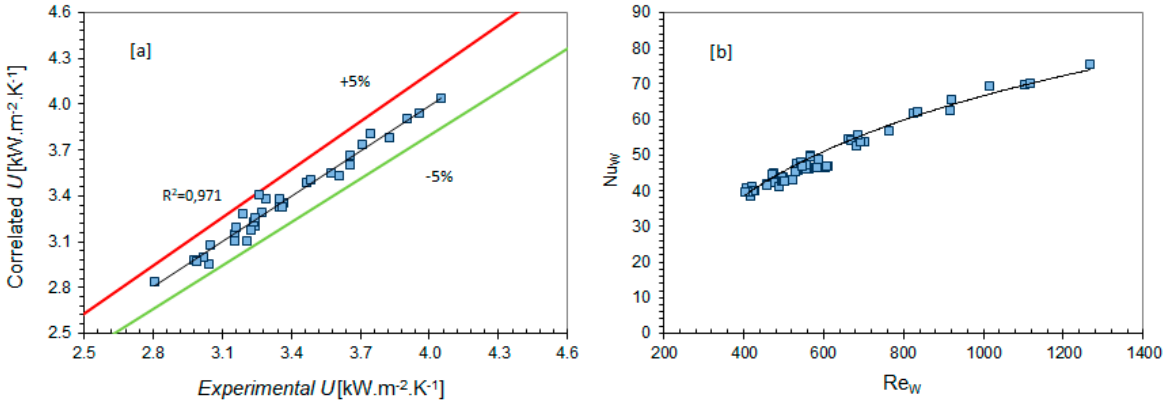

Figure 5. (**a**) Predicted U vs. experimental U and (**b**) Nusselt number vs. Reynolds number.

3.2. Semi-Empirical Model Results

This subsection presents the estimation of the temperatures and concentration at the inlet and outlet of each partial control volume of the PHE using the semi-empirical model (Mod). Modelling of the plate absorber was performed at a mass flow of 40 kg·h^{-1} in the solution side. Inlet operating

conditions were set as in Table 2. For comparison purposes, measured inlet and outlet conditions for temperature and solution concentration in the absorber are also depicted.

Simulation results were also contrasted to those from the theoretical model described by Cerezo et al. [14] (Mod [14]) at the same conditions. The model described in the literature considers the interface area between the NH_3/H_2O and the ammonia bubble vapour being absorbed. In addition, it employs several correlations reported in the literature from configurations where separated heat and mass transfer processes were considered. Moreover, it also included the correlations reported by Herbine and Perez-Blanco [15] to estimate the heat transfer between the NH_3/H_2O mixture and the wall.

Figure 6 illustrates the profiles of temperature and concentration along the PHE absorber. Results show that the measured and simulated outlet temperatures and concentrations in the PHE were reasonably close. For instance, Figure 6a shows that at a heat dissipation temperature of 40 °C at the PHE inlet, the temperature of the solution at the PHE outlet using the present model is 0.5 °C lower than that of the measured value, whereas the outlet temperature obtained with the model described by Cerezo et al. [14] is 2.2 °C lower. Moreover, at a water temperature equal to 35 °C, Figure 6d shows an immediate drop in the hot-side temperature when employing the semi-empirical model because of the greater potential for heat transfer due to the larger temperature difference. In this case, the solution-side temperature at the PHE outlet using the present model is 2.3 °C lower than that of the measured value, whereas the outlet temperature obtained with the model described in [14] is 3.2 °C below the measured value. In addition, Figure 6a,d shows that the water-side temperatures at the PHE absorber outlet follow a linear trend in both models, however, the present model approach was closer to the measured value.

As regards Figure 6b,e, the outlet concentration estimated with the model described in [14] is closer to the measured values in comparison to that of the semi-empirical model. It is then observed that the semi-empirical model tends to overestimate the solution concentration at the PHE absorber outlet, however, errors do not surpass 1.3%. Furthermore, Figure 6c,f presents the thermal load distribution along the control volumes of the PHE. Results show that both models predicted similar thermal load trends along the PHE, however, the thermal loads at the PHE outlet estimated with the semi-empirical model are closer to those of the measured values.

The total absorption mass flux obtained from the semi-empirical model and that calculated from the experiments present relative differences of 1.4% and 17.6%, at heat dissipation temperatures of 35 and 40 °C, respectively. For the thermal load, these relative differences are around 8.7% and 4.6%, at heat dissipation temperatures of 35 and 40 °C, respectively. Regarding the procedure described in [14], the relative differences of the total absorption mass flux with respect to the experimental values are around 11.2% and 16.8%, at heat dissipation temperatures of 35 and 40 °C, respectively. For the thermal load, these relative differences are around 16.7% and 24.9%, at heat dissipation temperatures of 35 and 40 °C, respectively.

In general, the estimations of the absorption mass flux and thermal load with the semi-empirical model were sufficiently close to the measured values. Although the liquid–vapor bubble interface area was not considered, approaches achieved were satisfactory.

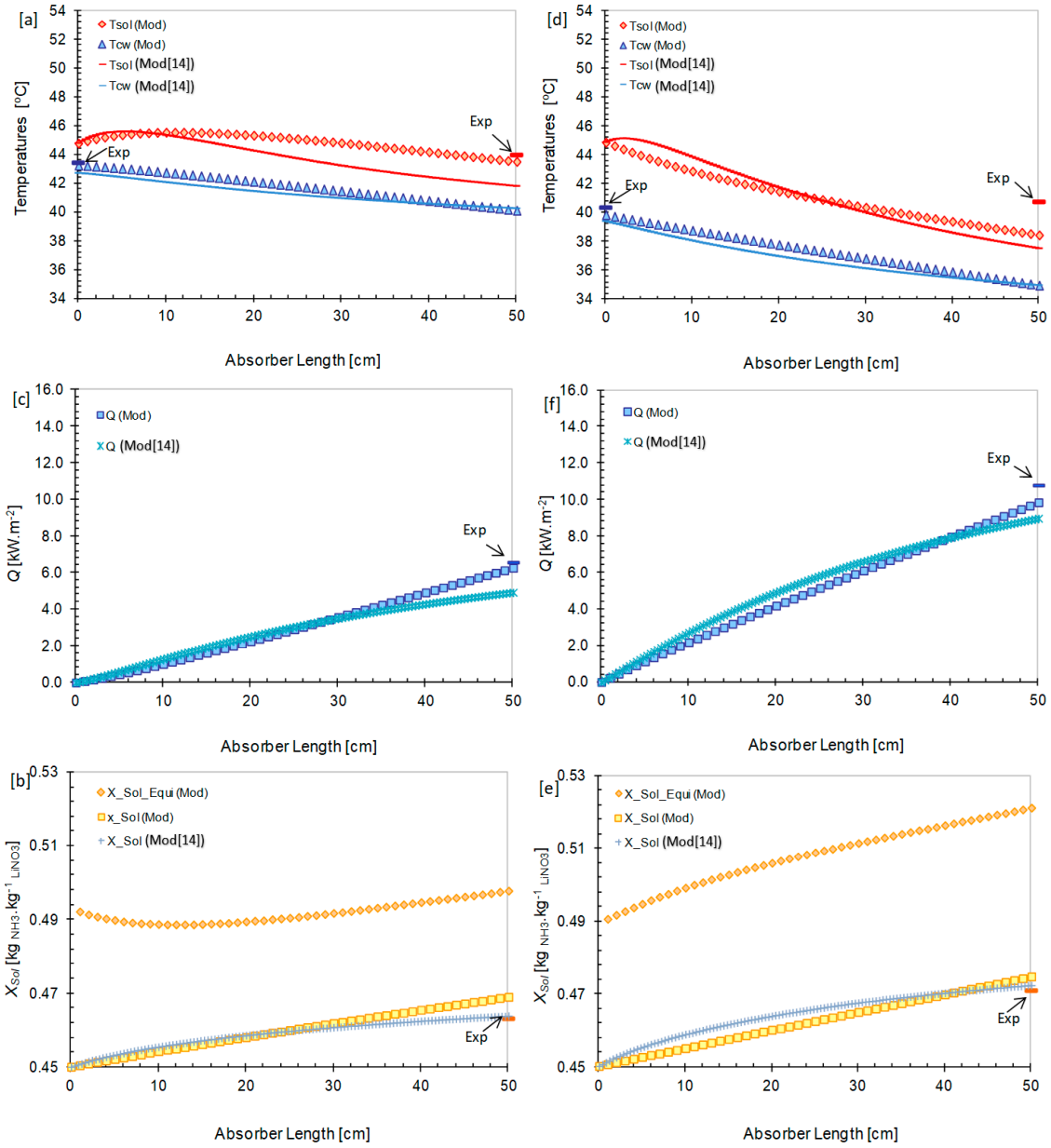

Figure 6. Profiles at a heat dissipation temperature of 40 °C for: (**a**) temperatures, (**b**) concentration, and (**c**) thermal load. Profiles at a heat dissipation temperature of 35 °C for: (**d**) temperatures, (**e**) concentration, and (**f**) thermal load.

3.3. Artificial Neural Network Results

In this subsection, the neural network model configuration and results are presented. As mentioned in Section 2.3, six input parameters at the absorber inlet were selected: absorber pressure (P_{Sol}), solution temperature (T_{Sol}), solution mass flow rate ($\dot{m}_{Sol}$), solution concentration (x_{Sol}), water-side temperature (T_{Cw}), and water-side flow rate (V_{Cw}). As output parameters, three performance parameters were selected to assess the NH_3 absorption phenomenon: the solution-side heat transfer coefficient (h_{Sol}), the absorption mass flux (F_{AB}), and the solution-side mass transfer coefficient (k_m). The ANN model was designed in three steps: learning, validation, and evaluation of the model. The learning step included training and design of the neural network. Moreover, the back-propagation technique was used for the ANN training. The training process finished when the relative difference between the ANN output data and the measured values (target) corresponded to the tolerance set. Different network designs

were tested to obtain the best correlation between the output data and the targets, and the minimum number of neurons. Therefore, each ANN design was assessed using the linear regression coefficient (R^2) and the root mean square error (rmse).

Figure 7 shows the final structure design of the ANN used to assess the H-type plate bubble absorber performance. Training results showed that a neural network employing a hidden layer with five neurons is a suitable structure for a satisfactory prediction of the selected parameters. As a result, a 6-5-3 ANN structure was defined as shown in Figure 7. Therefore, it consists of six neurons in the input layer, five neurons in the hidden layer, and three neurons in the output layer. When the number of processing neurons was reduced to fewer than five, the linear regression coefficient dropped. In addition, when the number of neurons was increased, no improvement in the linear regression coefficient was obtained. For instance, when the number of processing neurons was set to four, the linear regression coefficient dropped to 0.9096, 0.9429, and 0.8561, for the absorption mass flux, solution heat transfer coefficient, and mass transfer coefficient, respectively. By comparison, when the number of processing neurons was set to six, the linear regression coefficients were 0.9735, 0.9401, and 0.8968, for the absorption mass flux, solution heat transfer coefficient, and mass transfer coefficient, respectively.

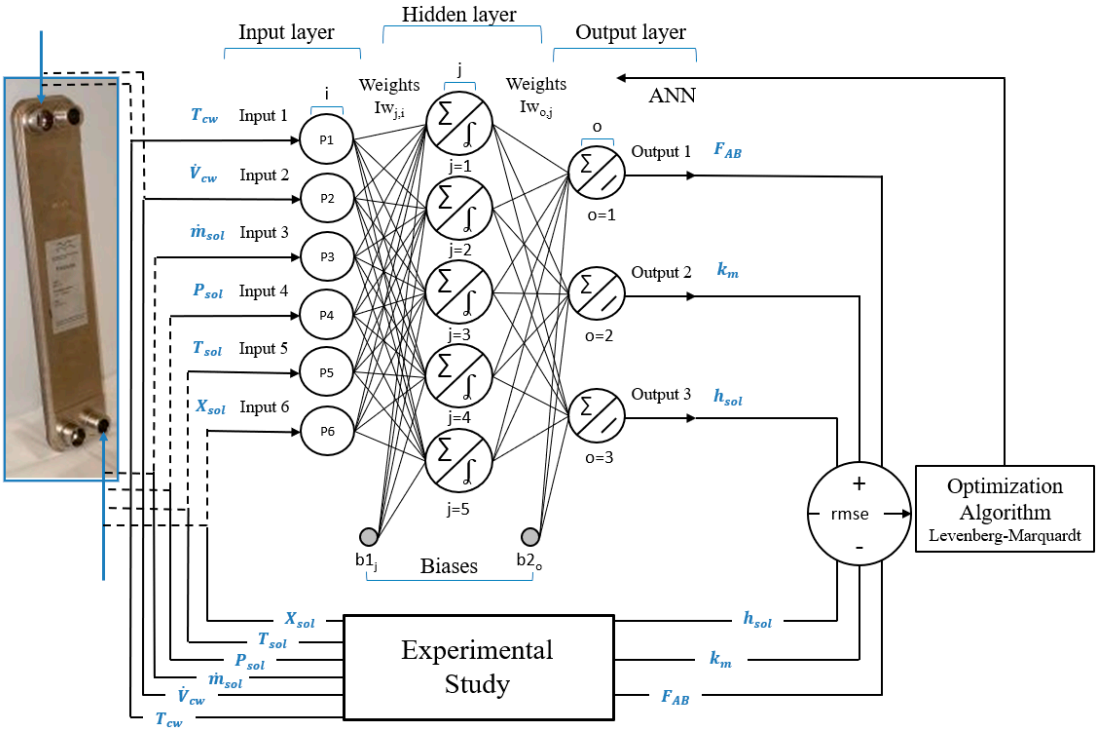

Figure 7. Design of the artificial neural network (ANN) structure used to assess the PHE absorber.

Equation (19) was used to predict the selected parameters for the evaluation of the NH_3 absorption process in the H-type PHE. In this equation, i refers to the inputs (i = 6), j refers to the neurons defined in the hidden layer (j = 5), P_i refers to the input "i" normalized, IW is the weight matrix in the hidden layer, LW is the weight matrix in the output layer, b_1 and b_2 refer to the bias in hidden and output layers, respectively; a refers to the output parameters and o refers to the selected output. For instance, o = 1 stands for the output $a_1 = F_{AB}$, o = 2 to k_m, o = 3 to h_{sol}.

$$a_o = \sum_{j=1}^{J}\left[LW_{o,j}\left(\frac{2}{1+exp\left(-2\left(\sum_{i=1}^{I} IW_{j,i}P_i + b1_j\right)\right)} - 1\right)\right] + b2_o \quad (19)$$

Table 3 shows the results from the ANN training process to model the selected parameters which allow assessment of the plate bubble absorber. It contains the weights and biases of the ANN finally resulting from the simulation study. Equations (20) to (25) show a sample of the calculations conducted for the output parameter 1 (o = 1). Parameter 1 refers to the absorption mass flux (F_{AB}). Therefore, this output depends on the inputs, the weights, and the biases as shown below:

$$F_{AB} = 2\left[\frac{LW_{1,1}}{1+exp(n_1)} + \frac{LW_{1,2}}{1+exp(n_2)} + \frac{LW_{1,3}}{1+exp(n_3)} + \frac{LW_{1,4}}{1+exp(n_4)} + \frac{LW_{1,5}}{1+exp(n_5)}\right] - (LW_{1,1} + LW_{1,2} + LW_{1,3} + LW_{1,4} + LW_{1,5}) + b2_1 \quad (20)$$

where n_1, n_2, n_3, n_4, and n_5 are determined from Equations (21) to (25).

$$n_1 = -2[IW_{1,1}P_1 + IW_{1,2}P_2 + IW_{1,3}P_3 + IW_{1,4}P_4 + IW_{1,5}P_5 + IW_{1,6}P_6 + b1_1] \quad (21)$$

$$n_2 = -2[IW_{2,1}P_1 + IW_{2,2}P_2 + IW_{2,3}P_3 + IW_{2,4}P_4 + IW_{2,5}P_5 + IW_{2,6}P_6 + b1_2] \quad (22)$$

$$n_3 = -2[IW_{3,1}P_1 + IW_{3,2}P_2 + IW_{3,3}P_3 + IW_{3,4}P_4 + IW_{3,5}P_5 + IW_{3,6}P_6 + b1_3] \quad (23)$$

$$n_4 = -2[IW_{4,1}P_1 + IW_{4,2}P_2 + IW_{4,3}P_3 + IW_{4,4}P_4 + IW_{3,5}P_5 + IW_{4,6}P_6 + b1_4] \quad (24)$$

$$n_5 = -2[IW_{5,1}P_1 + IW_{5,2}P_2 + IW_{5,3}P_3 + IW_{5,4}P_4 + IW_{3,5}P_5 + IW_{5,6}P_6 + b1_5] \quad (25)$$

Table 3. Weights and biases of the artificial neural network.

Hidden Layer						
Matrix of Weights ($IW_{j,i}$)						Bias ($b_{1,j}$)
4.59	-6.04×10^{-1}	6.11×10^{-1}	-4.61×10^{-1}	4.04	1.36	−4.11
3.12	1.06	1.19	4.85×10^{-1}	2.86	4.94	1.57
5.60	2.14	4.92×10^{-1}	4.80×10^{-1}	2.61	3.86	−1.33
2.17	1.17	-2.49×10^{-1}	-6.02×10^{-1}	-4.86×10^{-1}	5.10×10^{-1}	6.52×10^{-1}
1.51	6.00	2.16	4.76	4.87	6.90×10^{-1}	1.14×10^{1}
Output Layer						
Matrix of Weights ($LW_{o,j}$)						Bias ($b_{2,o}$)
-4.14×10^{-4}	1.52×10^{-3}	5.26×10^{-5}	3.74×10^{-3}	-3.90×10^{-3}		5.62×10^{-3}
-3.34×10^{-1}	4.22×10^{-1}	-1.31×10^{-1}	1.18	1.66		1.83
3.45	-4.09×10^{-1}	4.62×10^{-1}	5.53×10^{-1}	-8.43×10^{-1}		6.77

The experimental and estimated values using the present model were contrasted to establish the model prediction accuracy. Figure 8 shows the estimated or correlated data vs experimental data for each output parameter (F_{AB}, h_{sol}, and k_m). The black lines represent the trends of the results. The results evidenced a satisfactory correlation between the experimental and simulated data. This highlights that the ANN developed is suitable for estimating the selected parameters to assess the PHE absorber.

The ANN model can represent the collected data with average deviations of 4.26%, 4.2%, and 1.74%, for the absorption mass flux, solution heat transfer coefficient, and mass transfer coefficient, respectively. Moreover, the ANN can satisfactorily predict 97% of absorption mass flux data at relative differences below 10%. Similarly, the ANN model can predict 90% and 97% of the solution heat transfer coefficient and mass transfer coefficient data, respectively, at relative differences below 10%. Values of the corresponding fit parameter, R^2, of the ANN model are indicated in Figure 8.

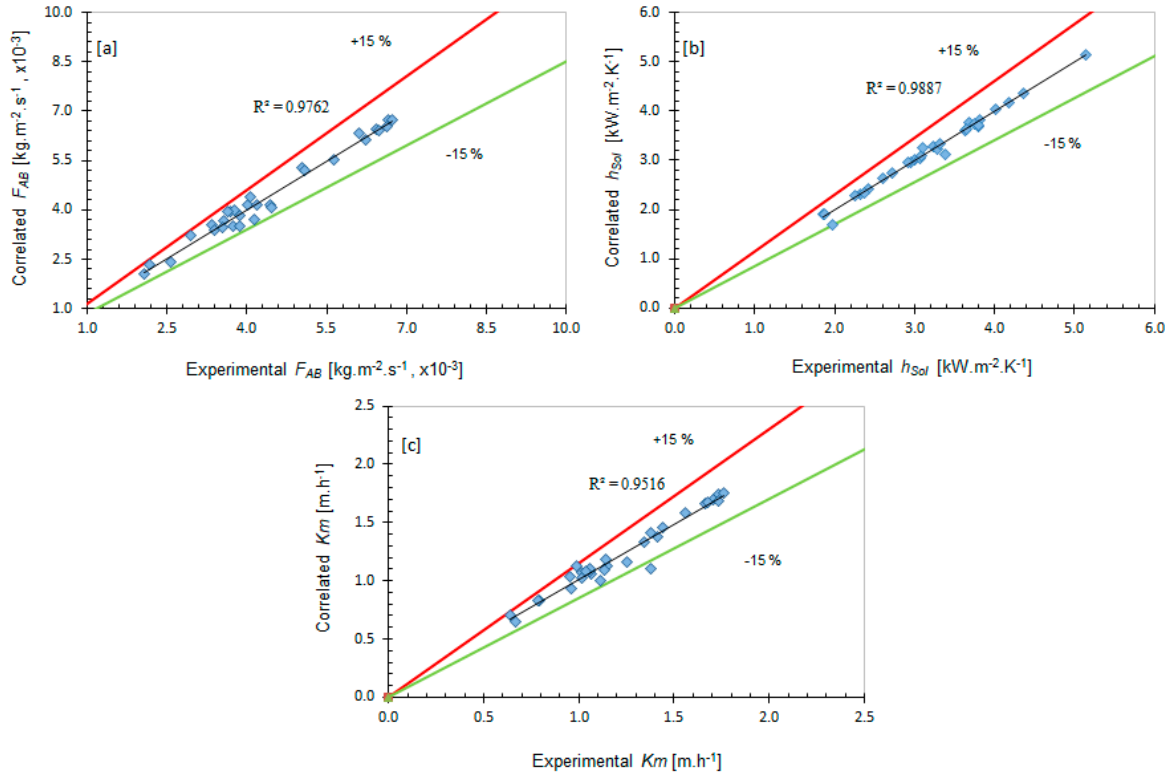

Figure 8. Experimental data vs. correlated data obtained using the ANN model: (**a**) absorption mass flux; (**b**) solution heat transfer coefficient; and (**c**) solution mass transfer coefficient.

3.4. Heat and Mass Transfer Rates Comparison

In this sub-section, the results of the absorption phenomenon in the H-type PHE using the semi-empirical model (Mod) and the ANN model (ANN) are contrasted with the available experimental results (Exp). This analysis was carried out under the same conditions; see Table 2. These conditions of operation correspond to those of a single effect absorption cooling system with $NH_3/LiNO_3$ driven by low-temperature heat sources at a chilled-water temperature of 5 °C.

Figure 9 shows that the semi-empirical and ANN models follow similar trends to those of experimental results. In addition, uncertainty errors for the experimental results are shown with bars with a resulting maximum value of ± 8% following the procedure recommended by the National Institute of Standards and Technology [50]. Figure 9 also presents the influence of the water-side temperature, solution-side mass flow, and water-side volumetric flow rate on the absorption mass flux and thermal load in the PHE. Furthermore, results in Figure 9a,c were collected at a water-side volumetric flow rate of 268 $L{\cdot}h^{-1}$, and results in Figure 9b,d were obtained at a solution-side mass flow of 40 $kg{\cdot}h^{-1}$.

Experimental results in Figure 9a,c correspond to water-side temperatures of 35 and 40 °C, and solution-side mass flows ranging from 10 to 50 $kg{\cdot}h^{-1}$. In these figures it can be observed that when the solution-side flow increases, the absorption mass flux rises from 0.0029 to 0.0061 $kg{\cdot}m^{-2}{\cdot}s^{-1}$ and from 0.0021 to 0.0044 $kg{\cdot}m^{-2}{\cdot}s^{-1}$ at the given temperatures, respectively. Moreover, the thermal load varied from 4.84 to 13.08 $kg{\cdot}m^{-2}$ and from 3.38 to 7.56 $kg{\cdot}m^{-2}$ for the same temperatures, respectively.

Experimental results in Figure 9b,d correspond to water-side temperatures of 35 and 40 °C, while the water-side flow ranges between 130 and 450 $l.h^{-1}$. In these figures can be noted that when the water-side flow increases, the absorption mass flux rises from 0.0056 to 0.0064 $kg{\cdot}m^{-2}{\cdot}s^{-1}$, and from 0.0033 to 0.0044 $kg{\cdot}m^{-2}{\cdot}s^{-1}$ at the specified temperatures, respectively. Thermal load varies between 10.31 and 13.2 $kW{\cdot}m^{-2}$, and between 6.02 and 7.97 $kW{\cdot}m^{-2}$ at the specified temperatures, respectively.

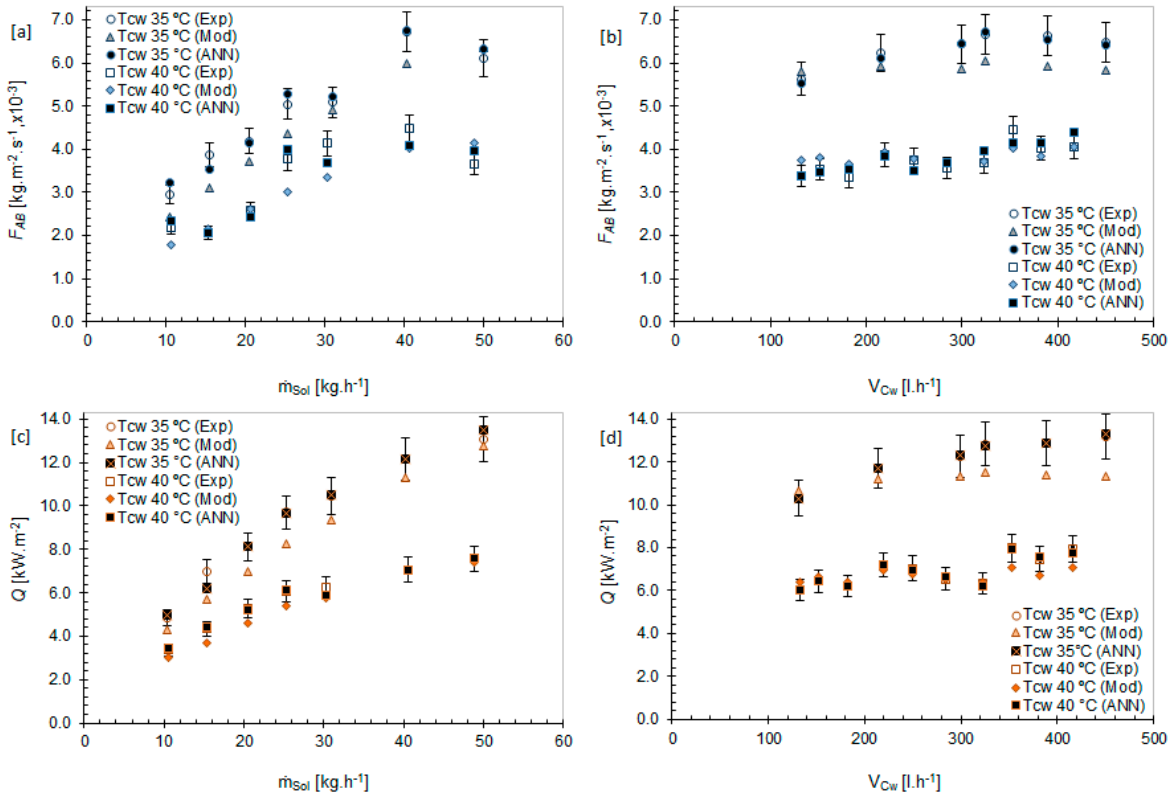

Figure 9. Experimental results vs. semi-empirical model and ANN model. Cooling-water temperature, solution mass flow, and cooling-water volumetric flow rate vs. (**a**,**b**) absorption mass flux, and (**c**,**d**) thermal load.

Results from the present study show that when the solution-side flow rises at the given values, the absorption process and heat transfer are positively affected in the corrugated PHE. This effect is obtained by the improvement in the solution and ammonia vapor mixing when increasing the solution flow regimen. Because the absorption process is exothermic, the higher the process, the more heat is released to the water-side and thus, the thermal load increases. It can also be observed that the vapor absorption improves as the water-side temperature at the PHE inlet decreases. This effect is associated with the improvement in the absorption and heat transfer potential; that is, the absorption capacity is enhanced when excess heat is released from the absorption process to the cooling water, allowing the solution to remain subcooled. As a result, this solution sub-cooling extends the difference between the current state and equilibrium state, and therefore, the solution can continue absorbing ammonia vapor. Regarding the effect of the water-side flow, only a slight increase in the heat and mass transport is observed. Therefore, the overall heat transfer coefficient is controlled by the solution-side heat transfer coefficient.

In general, the maximum and average relative differences between the semi-empirical and experimental models were 15.8% and 6.0%, respectively, for the absorption mass flux. In addition, 83.3% of the data showed a relative difference below 10.0%. In the case of the thermal load, the maximum and average relative differences were 12.5% and 6.4%, respectively. Results also showed that 86.7% of the data presented a relative difference below 10.0%. Figure 9 also shows that the relative differences between results from the experimental study and the semi-empirical models are more pronounced at a water-side temperature of 35 °C.

Predictions of the artificial neural network showed that the maximum and average relative differences between the ANN model and experimental results were around 10.8% and 4.3%, respectively, for the absorption mass flux. In addition, 90% of the data evidenced a relative difference below 9.0%. In the case of the thermal load, the maximum and average relative differences were 11.3% and 1.3%,

respectively. Results also showed that 97% of the thermal load data presented a relative difference below 9.0%.

Results confirmed that the semi-empirical model is suitable for estimating temperatures and concentration at the inlet and outlet of each partial control of volume in the PHE absorber, in addition to heat and mass transfer. As in the case of most heat and mass transfer models, this model requires the thermodynamics properties of the fluids and dimensions of the bubble absorber under study as inputs. Alternatively, the ANN model can estimate the absorption process phenomenon in the PHE absorber with lower errors compared to the semi-empirical model. Although internal details of the absorption process phenomenon are not needed, the ANN model is not suitable for the prediction of internal parameters, such as temperature and pressure profiles, or local heat and mass transfer details. It is finally highlighted that the ANN is a more effective method for prediction and control of the absorption process performance parameters in the studied configuration compared to the semi-empirical method. Furthermore, the semi-empirical method is preferable depending on the levels of internal/local heat and mass transfer details requirements. Finally, it is worth noting that, because the semi-empirical model uses dimensionless correlations, it could be adapted to other working fluids and slight variations in the absorber geometry, whereas the ANN model is specific to the configuration investigated in the present paper and within the ranges provided for the training process (see Tables 1 and 2) and thermophysical properties of $NH_3/LiNO_3$.

4. Conclusions

This paper presented the development and comparison of two models, a one-dimensional semi-empirical model and an ANN model, designed and developed to quantify the heat and mass transfer in an H-type PHE in bubble mode employing a $NH_3/LiNO_3$ mixture.

Correlations to estimate the solution-side heat transfer coefficient, mass transfer coefficient, and water-side heat transfer coefficient are proposed. Results from the numerical models, the semi-empirical and ANN models, were contrasted with experimental results and indicated the proposed approach was suitable. Moreover, the semi-empirical model provided a reasonable approach to internal temperature and concentration details; for instance, temperature and concentration at the PHE outlet were sufficiently close to the results obtained by experiment. Moreover, the ANN model allowed better estimation of the overall heat and mass transfer in the studied bubble absorber compared to that of the semi-empirical model. In addition, one of the advantages of the ANN is that there is no need for internal details of the absorption process and thermophysical properties, however, its application is limited to the configuration studied.

Results showed that the semi-empirical model was able to predict the absorption mass flux and thermal load with maximum differences of 15.8% and 12.5%, respectively, relative to the experimental results. In the case of the ANN model, the maximum relative difference was 10.8% and 11.3% for the absorption mass flux and thermal load, respectively. Moreover, the semi-empirical model is preferable when more details of the internal mass absorption of the absorber are needed.

Finally, results showed that the correlations developed and proposed provided a good prediction of local heat and mass transfer along the absorber. Analysis of the simulation results also demonstrated that both models can be practically applied to the design of bubble plate absorbers with $NH_3/LiNO_3$ mixtures.

Author Contributions: Conceptualization, C.A., M.E.A., M.V. and M.B.; Formal analysis, C.A.; Investigation, C.A.; Methodology, C.A., M.E.A., M.V. and M.B.; Software, C.A. and M.E.A.; Validation, C.A.; Writing—original draft, C.A. and M.E.A.; Writing—review & editing, C.A. and M.B.; Supervision, M.V. and M.B.; Funding acquisition, M.V. and M.B. All authors have read and agreed to the published version of the manuscript.

Funding: This study was part of an R&D project funded by the Spanish Ministry of Science and Innovation (ENE2008-00863).

Conflicts of Interest: The author declares no conflict of interest.

Nomenclature

A	heat transfer area, m^2
Ap	Pass area, m^2
Cp	heat capacity, $kJ \cdot kg^{-1} \cdot K^{-1}$
D	diameter, m
dl	differential length, m
$d\dot{Q}$	differential thermal load, kW
dTa	differential transfer area, m^2
e	wall thickness, m
F	NH_3 absorption mass flux, $kg \cdot m^{-2} \cdot s^{-1}$
h	enthalpy, $kJ \cdot kg^{-1}$
Km	mass transfer coefficient, $m \cdot h^{-1}$
LMTD	logarithmic mean temperature difference, °C
LMXD	logarithmic mean concentration difference
$\dot{m}$	mass flow rate, $kg \cdot s^{-1}$
MSE	mean square error
Nu	Nusselt number
NV	Needle valve
P	pressure, kPa
Pr	Prandtl number
Pw	wet perimeter, m
Q	thermal load per unit of area, $kW \cdot m^{-2}$
R	resistance
Re	Reynolds number
Sc	Schmidt number
Sh	Sherwood number
T	temperature, °C
U	overall heat transfer coefficient, $kW \cdot m^{-2} \cdot K^{-1}$
V	volumetric flow rate, $m^3 \cdot h^{-1}$
x	NH_3 concentration, $kg_{NH3} \cdot kg^{-1}{}_{NH3/LiNO3}$

Subscripts

AB	absorber
Cw	cooling water
Eq	equilibrium
Exp	experimental result
h	hydraulic
In	absorber inlet
$LiNO_3$	Lithium nitrate
m	average
NH_3	ammonia
Out	absorber outlet
Sat	saturation state
Sol	solution of $NH_3/LiNO_3$
Steel	stainless steel
Vap	ammonia vapour

Greek Letters

λ	thermal conductivity, $kW \cdot m^{-1} \cdot K^{-1}$
α	heat transfer coefficient, $kW \cdot m^{-2} \cdot K^{-1}$

References

1. Amaris, C.; Vallès, M.; Bourouis, M. Vapour absorption enhancement using passive techniques for absorption cooling/heating technologies: A review. *Appl. Energy* **2018**, *231*, 826–853. [CrossRef]
2. Aggarwal, M.K.; Agarwal, R.S. Thermodynamic properties of lithium nitrate-ammonia mixtures. *Int. J. Energy Res.* **1986**, *10*, 59–68. [CrossRef]
3. Infante Ferreira, C.A. Thermodynamic and physical property data equations for ammonia-lithium nitrate and ammonia-sodium thiocyanate solutions. *Sol. Energy* **1984**, *32*, 231–236. [CrossRef]
4. Abdulateef, J.M.; Sopian, K.; Alghoul, M.A. Optimum design for solar absorption refrigeration systems and comparison of the performances using ammonia-water, ammonia-lithium nitrate and ammonia-sodium thiocyanate solutions. *Int. J. Mech. Mater. Eng.* **2008**, *3*, 17–24.
5. Infante Ferreira, C.A. Operating characteristics of NH_3–$LiNO_3$ and NH_3–NaSCN absorption refrigeration machines. In Proceedings of the 19th Int. Congr. Refrig, the Hague, The Netherlands, 20–25 August 1995; pp. 321–328.
6. Ayala, R.; Frías, J.L.; Lam, L.; Heard, C.L.; Holland, F.A. Experimental assessment of an ammonia/lithium nitrate absorption cooler operated on low temperature geothermal energy. *Heat Recover. Syst. CHP* **1994**, *14*, 437–446. [CrossRef]
7. Heard, C.L.; Ayala, R.; Best, R. An experimental comparison of an absorption refrigerator using ammonia/water and ammonia/lithium nitrate. In Proceedings of the International Sorption Heat Pump Conference, Montreal, QC, Canada, 17–20 September 1996; pp. 245–252.
8. Oronel, C.; Amaris, C.; Bourouis, M.; Vallès, M. Heat and mass transfer in a bubble plate absorber with $NH_3/LiNO_3$ and $NH_3/(LiNO_{3+}$ $H_2O)$ mixtures. *Int. J. Therm. Sci.* **2013**, *63*. [CrossRef]
9. Amaris, C.; Bourouis, M.; Vallès, M. Effect of advanced surfaces on the ammonia absorption process with $NH_3/LiNO_3$ in a tubular bubble absorber. *Int. J. Heat Mass Transf.* **2014**, *72*. [CrossRef]
10. Amaris, C.; Bourouis, M.; Vallès, M. Passive intensification of the ammonia absorption process with NH3/LiNO3using carbon nanotubes and advanced surfaces in a tubular bubble absorber. *Energy* **2014**, *68*, 519–528. [CrossRef]
11. Kang, Y.T.; Akisawa, A.; Kashiwagi, T. Analytical investigation of two different absorption modes: Falling film and bubble types. *Int. J. Refrig.* **2000**, *23*, 430–443. [CrossRef]
12. Castro, J.; Oliet, C.; Rodríguez, I.; Oliva, A. Comparison of the performance of falling film and bubble absorbers for air-cooled absorption systems. *Int. J. Therm. Sci.* **2009**, *48*, 1355–1366. [CrossRef]
13. Infante Ferreira, C.A. Combined momentum, heat and mass transfer in vertical slug flow absorbers. *Int. J. Refrig.* **1985**, *8*, 326–334. [CrossRef]
14. Cerezo, J.; Best, R.; Romero, R.J. A study of a bubble absorber using a plate heat exchanger with NH_3–H_2O, NH_3–$LiNO_3$ and NH_3–NaSCN. *Appl. Therm. Eng.* **2011**, *31*, 1869–1876. [CrossRef]
15. Herbine, G.S.; Perez-Blanco, H. Model of an ammonia-water bubble absorber. *ASHRAE Trans.* **1995**, *101*, 1324–1334.
16. Fernández-Seara, J.; Sieres, J.; Rodríguez, C.; Vázquez, M. Ammonia–water absorption in vertical tubular absorbers. *Int. J. Therm. Sci.* **2005**, *44*, 277–288. [CrossRef]
17. Fernández-Seara, J.; Uhía, F.J.; Sieres, J. Analysis of an air cooled ammonia–water vertical tubular absorber. *Int. J. Therm. Sci.* **2007**, *46*, 93–103. [CrossRef]
18. Kang, Y.T.; Christensen, R.N.; Kashiwagi, T. Ammonia-Water bubble absorber with a plate heat exchanger. *Int. J. Refrig.* **1998**, *104*, 956–966.
19. Lee, J.-C.; Lee, K.-B.; Chun, B.-H.; Lee, C.H.; Ha, J.J.; Kim, S.H. A study on numerical simulations and experiments for mass transfer in bubble mode absorber of ammonia and water. *Int. J. Refrig.* **2003**, *26*, 551–558. [CrossRef]
20. Cerezo, J.; Best, R.; Bourouis, M.; Coronas, A. Comparison of numerical and experimental performance criteria of an ammonia–water bubble absorber using plate heat exchangers. *Int. J. Heat Mass Transf.* **2010**, *53*, 3379–3386. [CrossRef]
21. Wang, M.; He, L.; Infante Ferreira, C.A. Ammonia absorption in ionic liquids-based mixtures in plate heat exchangers studied by a semi-empirical heat and mass transfer framework. *Int. J. Heat Mass Transf.* **2019**, *134*, 1302–1317. [CrossRef]

22. Sujatha, K.S.; Mani, A.; Srinivasa Murthy, S. Finite element analysis of a bubble absorber. *Int. J. Numer. Methods Heat Fluid Flow* **1997**, *7*, 737–750. [CrossRef]
23. Sujatha, K.S.; Mani, A.; Srinivasa, M.S. Analysis of a bubble absorber working with R22 and five organic absorbents. *Heat Mass Transf. Stoffuebertragung* **1997**, *32*, 255–259. [CrossRef]
24. Merrill, T.L.; Perez-Blanco, H. Combined heat and mass transfer during bubble absorption in binary solutions. *Int. J. Heat Mass Transf.* **1997**, *40*, 589–603. [CrossRef]
25. Terasaka, K.; Oka, J.; Tsuge, H. Ammonia absorption from a bubble expanding at a submerged orifice into water. *Chem. Eng. Sci.* **2002**, *57*, 3757–3765. [CrossRef]
26. Kim, J.-K.; Park, C.W.; Kang, Y.T. The effect of micro-scale surface treatment on heat and mass transfer performance for a falling film H_2O/LiBr absorber. *Int. J. Refrig.* **2003**, *26*, 575–585. [CrossRef]
27. Elperin, T.; Fominykh, A. Four stages of the simultaneous mass and heat transfer during bubble formation and rise in a bubbly absorber. *Chem. Eng. Sci.* **2003**, *58*, 3555–3564. [CrossRef]
28. Suresh, M.; Mani, A. Heat and mass transfer studies on R134a bubble absorber in R134a/DMF solution based on phenomenological theory. *Int. J. Heat Mass Transf.* **2010**, *53*, 2813–2825. [CrossRef]
29. Staicovici, M.D. A non-Equilibrium phenomenological theory of the mass and heat transfer in physical and chemical interactions: Part II—Modeling of the NH_3/H_2O bubble absorption, analytical study of absorption and experiments. *Int. J. Heat Mass Transf.* **2000**, *43*, 4175–4188. [CrossRef]
30. Staicovici, M.D. A non-Equilibrium phenomenological theory of the mass and heat transfer in physical and chemical interactions: Part I—Application to NH_3/H_2O and other working systems. *Int. J. Heat Mass Transf.* **2000**, *43*, 4153–4173. [CrossRef]
31. Kaji, R.; Azzopardi, B.J.; Lucas, D. Investigation of flow development of co-current gas–liquid vertical slug flow. *Int. J. Multiph. Flow* **2009**, *35*, 335–348. [CrossRef]
32. Muniz, M.; Sommerfeld, M. On the force competition in bubble columns: A numerical study. *Int. J. Multiph. Flow* **2020**, *128*. [CrossRef]
33. Kalogirou, S.A. Artificial neural networks in renewable energy systems applications: A review. *Renew. Sustain. Energy Rev.* **2000**, *5*, 373–401. [CrossRef]
34. Mohanraj, M.; Jayaraj, S.; Muraleedharan, C. Applications of artificial neural networks for refrigeration, air-conditioning and heat pump systems—A review. *Renew. Sustain. Energy Rev.* **2012**, *16*, 1340–1358. [CrossRef]
35. Sözen, A.; Akçayol, M.A. Modelling (using artificial neural-networks) the performance parameters of a solar-driven ejector-absorption cycle. *Appl. Energy* **2004**, *79*, 309–325. [CrossRef]
36. Manohar, H.J.; Saravanan, R.; Renganarayanan, S. Modelling of steam fired double effect vapour absorption chiller using neural network. *Energy Convers. Manag.* **2006**, *47*, 2202–2210. [CrossRef]
37. Chow, T.T.; Zhang, G.Q.; Lin, Z.; Song, C.L. Global optimization of absorption chiller system by genetic algorithm and neural network. *Energy Build.* **2002**, *34*, 103–109. [CrossRef]
38. Hernández, J.A.; Juárez-Romero, D.; Morales, L.I.; Siqueiros, J. COP prediction for the integration of a water purification process in a heat transformer: With and without energy recycling. *Desalination* **2008**, *219*, 66–80. [CrossRef]
39. Labus, J.; Bruno, J.C.; Coronas, A. Performance analysis of small capacity absorption chillers by using different modeling methods. *Appl. Therm. Eng.* **2013**, *58*, 305–313. [CrossRef]
40. Álvarez, M.E.; Hernández, J.A.; Bourouis, M. Modelling the performance parameters of a horizontal falling film absorber with aqueous (lithium, potassium, sodium) nitrate solution using artificial neural networks. *Energy* **2016**, *102*, 313–323. [CrossRef]
41. Amaris, C. Intensification of NH_3 Bubble Absorption Process Using Advanced Surfaces and Carbon Nanotubes for $NH_3/LiNO_3$ Absorption Chillers. Ph.D. Thesis, Universitat Rovira i Virgili, Tarragona, Spain, 2013.
42. Libotean, S.; Salavera, D.; Valles, M.; Esteve, X.; Coronas, A. Vapor-liquid equilibrium of ammonia + lithium nitrate + water and ammonia + lithium nitrate solutions from (293.15 to 353.15) K. *J. Chem. Eng. Data* **2007**, *52*, 1050–1055. [CrossRef]
43. Libotean, S.; Martín, A.; Salavera, D.; Valles, M.; Esteve, X.; Coronas, A. Densities, viscosities, and heat capacities of ammonia + lithium nitrate and ammonia + lithium nitrate + water solutions between (293.15 and 353.15) K. *J. Chem. Eng. Data* **2008**, *53*, 2383–2388. [CrossRef]

44. Cuenca, Y.; Vernet, A.; Vallès, M. Thermal conductivity enhancement of the binary mixture (NH_3+ $LiNO_3$) by the addition of CNTs. *Int. J. Refrig.* **2014**, *41*, 113–120. [CrossRef]
45. Haltenberger, W. Enthalpy-Concentration charts from vapor pressure data. *Ind. Eng. Chem.* **1939**, *31*, 783–786. [CrossRef]
46. McNeely, L.A. Thermodynamic properties of aqueous solutions of lithium bromide. *ASHRAE Trans.* **1979**, *85*, 413–434.
47. Infante Ferreira, C.A. Vertical Tubular Absorbers for Ammonia—Salt Absorption Refrigeration. Ph.D. Thesis, Delft University of Technology, Delft, The Netherlands, 1985.
48. Despagne, F. Neural networks in multivariate calibration. *Analyst* **1998**, *123*. [CrossRef] [PubMed]
49. Cerezo, J. Estudio Del Proceso De Absorción Con Amoníaco-Agua en Intercambiadores De Placas Para Equipos de Refrigeración Por Absorción. Ph.D. Thesis, Universitat Rovira i Virgili, Tarragona, Spain, 2006.
50. Taylor, B.N.; Kuyatt, C.E. *Guidelines for Evaluating and Expressing the Uncertainty of NIST Measurement Results, Technical Note 1297*; Diane Publishing: Darby, PA, USA, 1994.